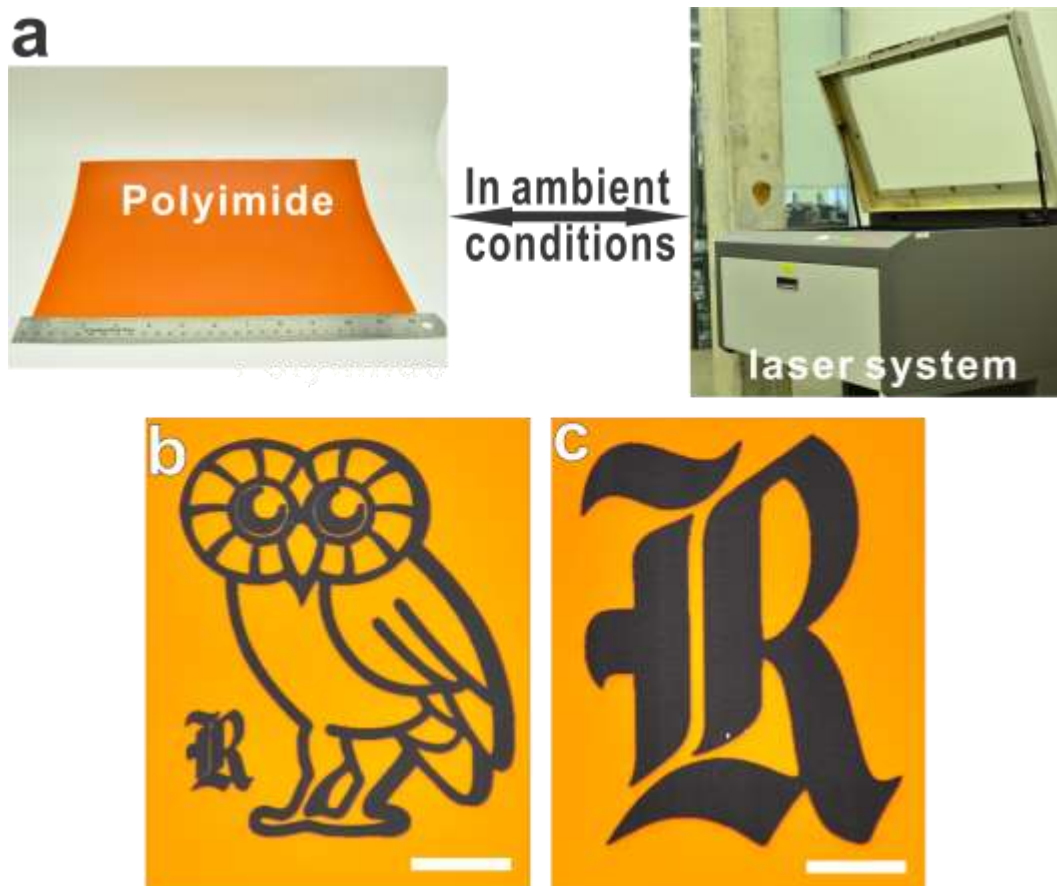
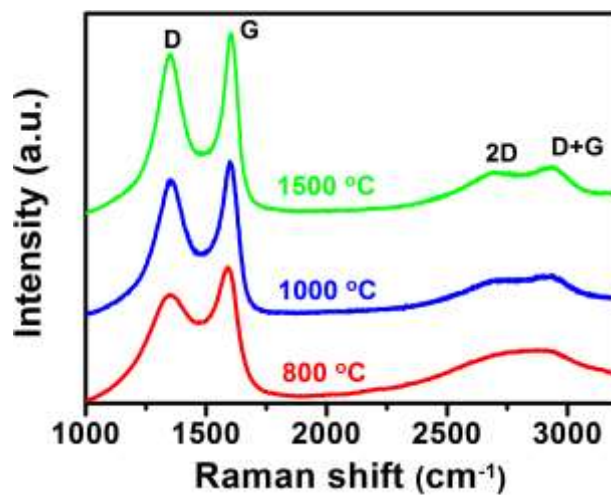


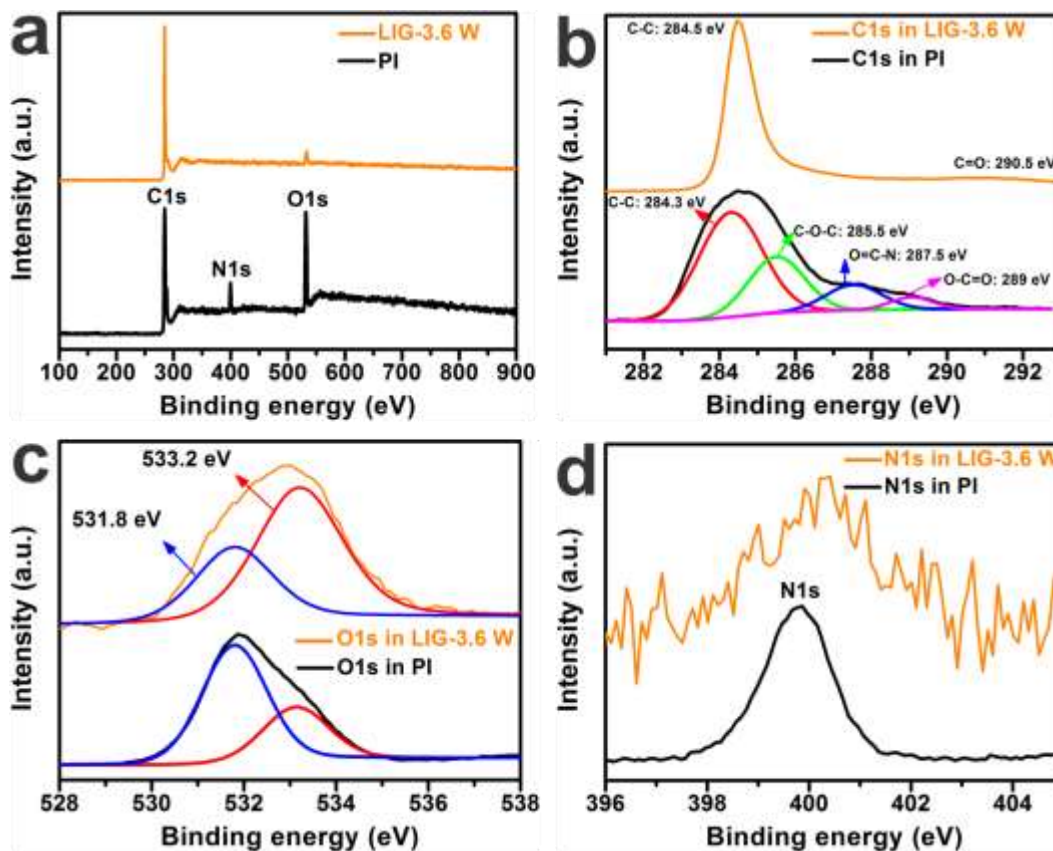
## Supplementary Figures



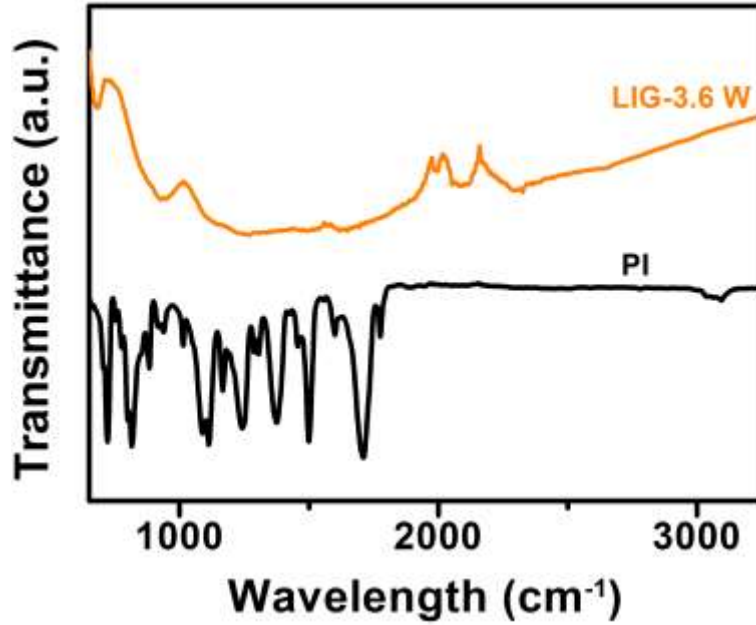
**Supplementary Figure 1 | Materials and equipment for production of LIG from PI by laser scribing.** **a**, Photographs of commercial Kapton PI sheets (left) with a 30 cm ruler, and the laser cutting system (right). **b** and **c**, Photographs of an owl and a letter R patterned on PI substrates; scale bar, 5 mm. In **b** and **c**, black contrast is LIG after exposure to the laser, while the lighter background corresponds to PI. The laser power used to scribe the images was 3.6 W.



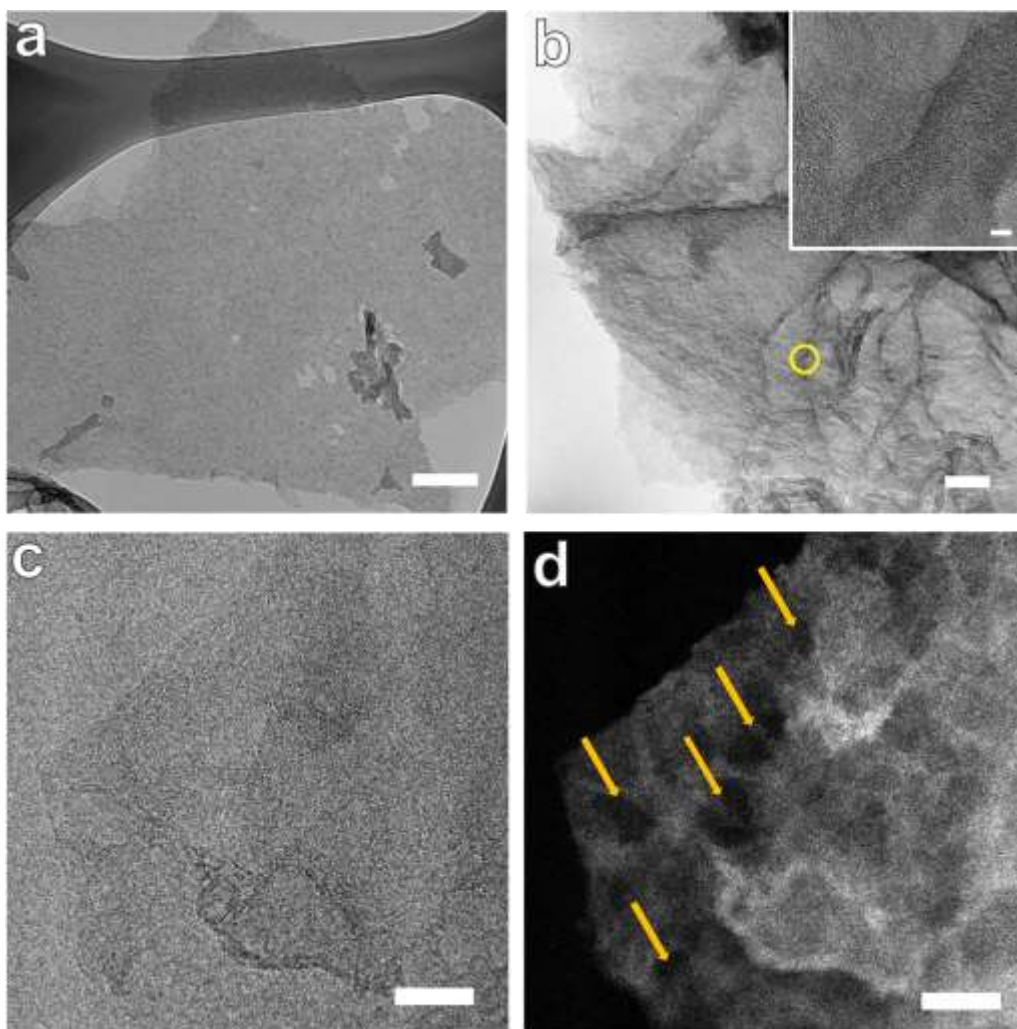
**Supplementary Figure 2 | Raman spectra of control samples.** PI sheets were carbonized in a furnace under Ar flow of 300 sccm for 3 h with annealing temperatures: 800 °C, 1000 °C and 1500 °C. Raman spectra show that these carbonized materials were glassy and amorphous carbon.



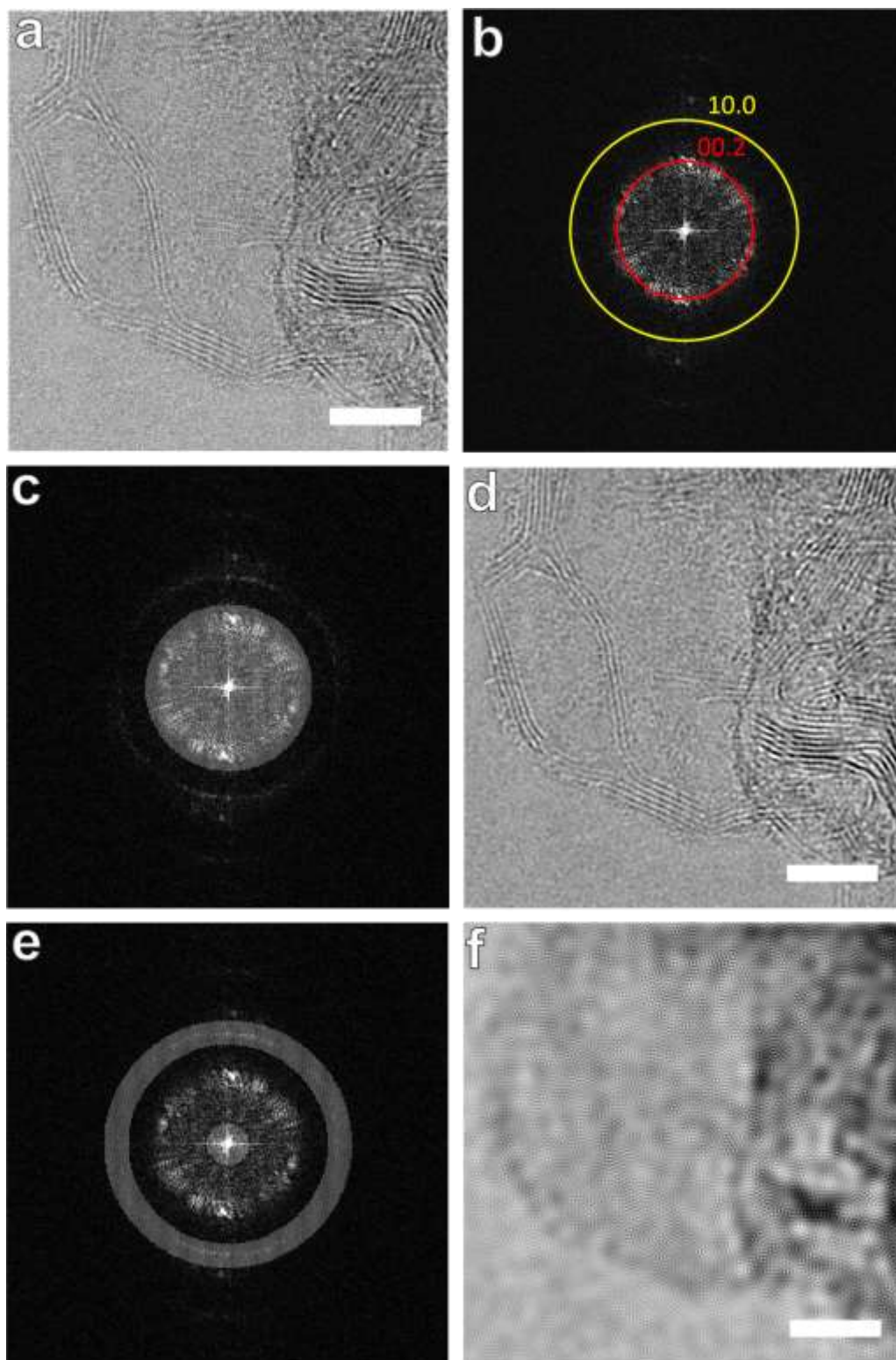
**Supplementary Figure 3 | XPS characterization of LIG-3.6 W films.** **a**, XPS surveys of LIG and PI. Comparison curves show that the oxygen and nitrogen peaks were significantly suppressed after PI was converted to LIG. **b**, High resolution C1s XPS spectrum of the LIG film and PI, showing the dominant C—C peak. The C—N, C—O and C=O peaks from PI were greatly reduced in the C1s XPS spectrum of LIG, which indicates that LIG was primarily  $sp^2$ -carbons. **c**, High resolution O1s XPS spectrum of a LIG-3.6 W film and PI. After laser conversion, the C—O (533.2 eV) peak becomes more dominant than C=O (531.8 eV). **d**, High resolution N1s XPS spectrum of a LIG-3.6 W film and PI. The intensity of the N1s peak was greatly reduced after laser exposure.



**Supplementary Figure 4 | FTIR spectra of LIG-3.6 W and PI films.** FTIR spectra of PI showing distinct peaks at 1090-1776 cm<sup>-1</sup>, corresponding to the well-defined stretching and bending modes of the C—O, C—N, and C=C bonds. After the laser scribing, a broad absorption from 1000 cm<sup>-1</sup> to 1700 cm<sup>-1</sup> shows that the laser scribing leads to a large variation in the local environment.

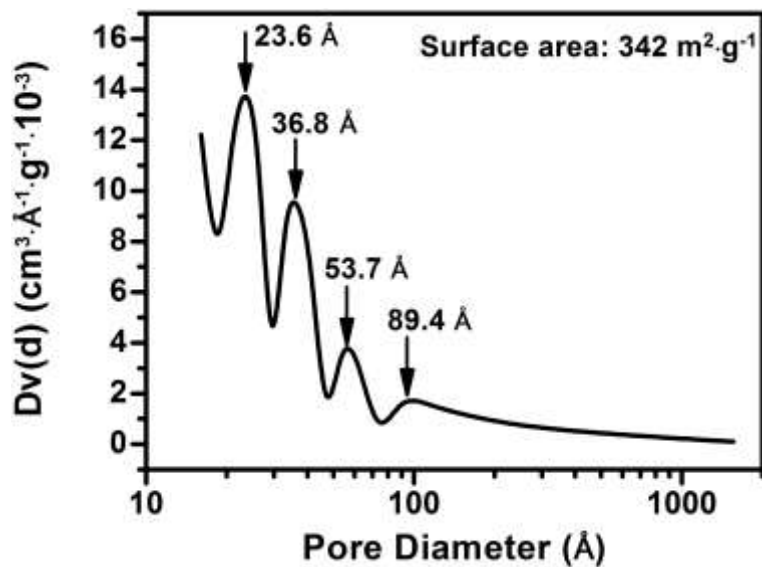


**Supplementary Figure 5 | TEM characterization of LIG-3.6 W flakes.** **a**, TEM image of a thin LIG flake atop a carbon grid; scale bar, 200 nm. **b**, TEM image of a thick LIG flake showing entangled tree-like ripples; scale bar, 100 nm. Inset is the HRTEM image of the yellow-circled region showing the mesoporous structures; scale bar, 5 nm. **c** and **d**, TEM images of LIG in bright and dark field view; scale bars, 10 nm. In dark field view, folded graphene containing several pores between 5 to 10 nm can be seen. These pores indicated in orange arrows in **d** result from curvature of the graphene layers induced by abundant pentagon-heptagon pairs<sup>1</sup>.



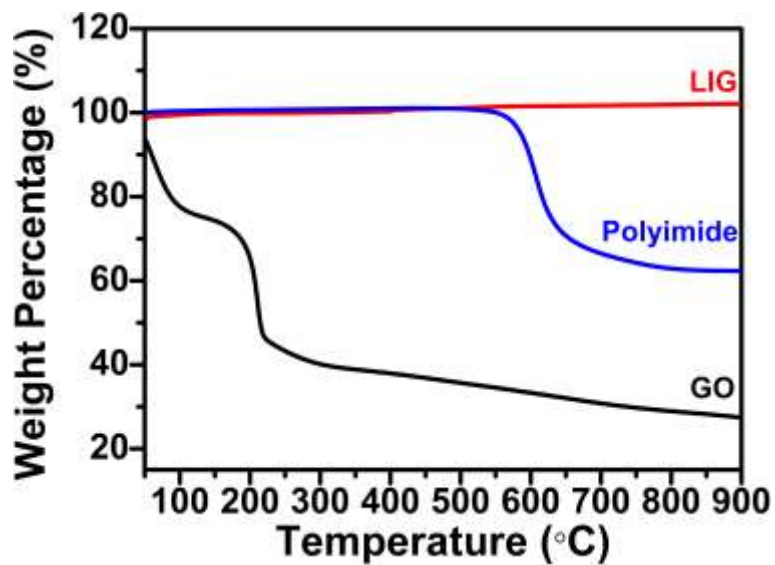
**Supplementary Figure 6 | TEM characterization of LIG-3.6 W flakes using filtering techniques.** **a**, The bright-field TEM image of the studied area; scale bar, 5 nm. **b**, FFT of the

LIG sample. The area has two distinct parts that can be seen on the indexed diffractogram FFT with the hexagonal crystal structure of carbon with lattice parameters  $a = 2.461 \text{ \AA}$  and  $c = 6.708 \text{ \AA}$ . The outer circle spots are reflections of the type (10.0) or (1.-1.0), corresponding to the basal plane of graphite 00.1. The layers are, however, very disordered and produce a rotational pattern with d-spacing of  $2.10 \text{ \AA}$ . The inner circle spots are type (00.2) corresponding to a d-spacing of  $3.35 \text{ \AA}$  of the folded layers of graphene containing the cavities. **c**, The filter uses the inner circle of type (00.2) spots and neglects the outer circle of type (10.0) spots. **d**, Corresponding filtered image from **c**; scale bar, 5 nm. The folded graphene structure was enhanced. **e**, The filter uses the outer circle of type (10.0) spots and neglects the inner circle of type (00.2) spots. **f**, Corresponding filtered image from **e**; scale bar, 5 nm. The disordered graphene structure was enhanced.

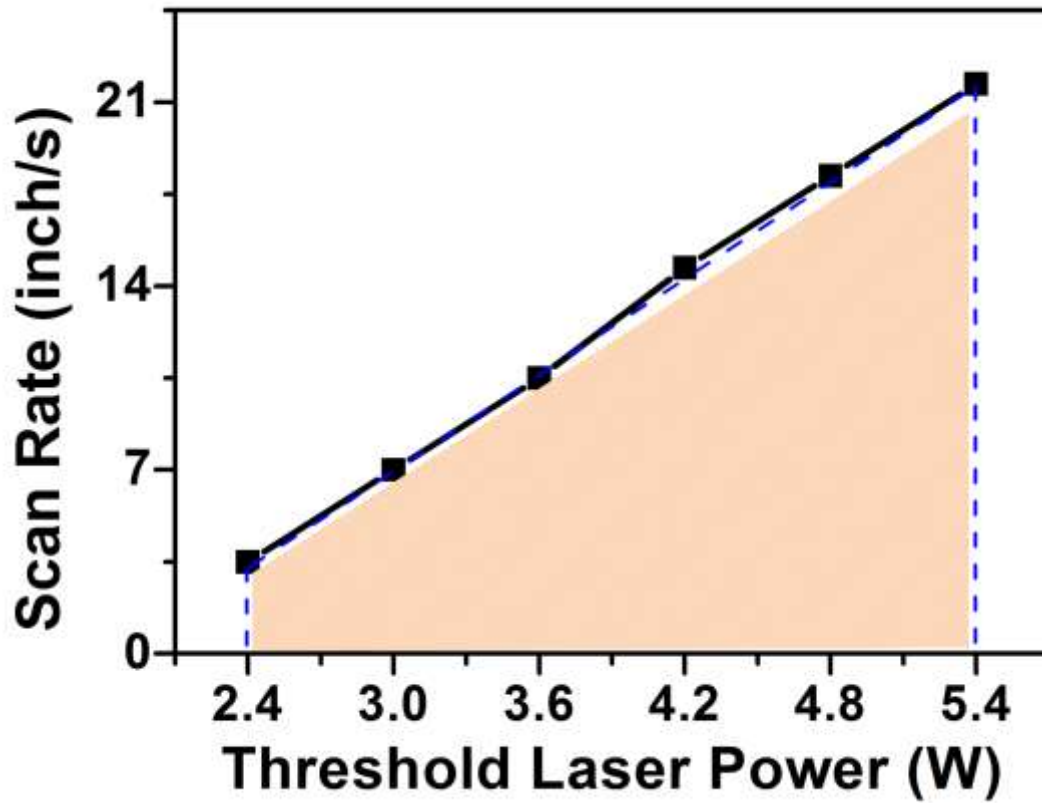


**Supplementary Figure 7 | BET specific surface area of LIG-3.6 W.** The surface area of this sample was  $\sim 342 \text{ m}^2 \cdot \text{g}^{-1}$ . Pore sizes are distributed at 2.36 nm, 3.68 nm, 5.37 nm and 8.94 nm.

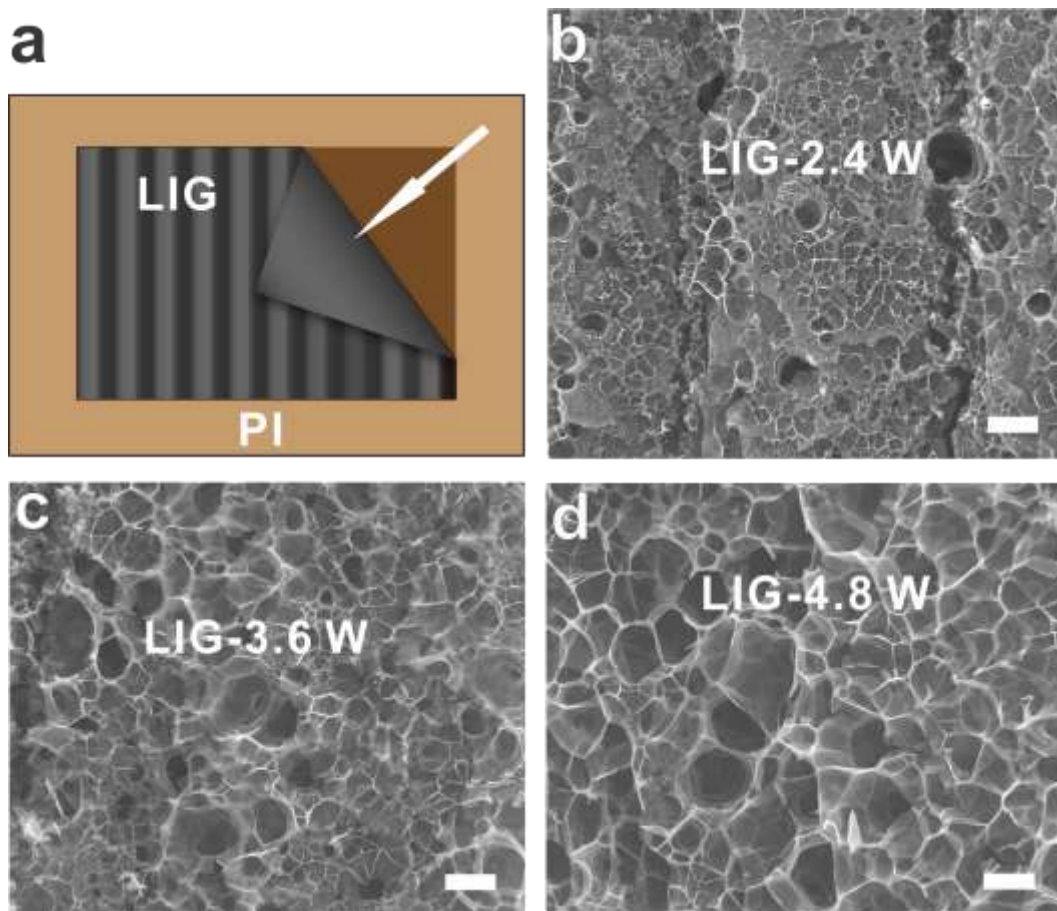




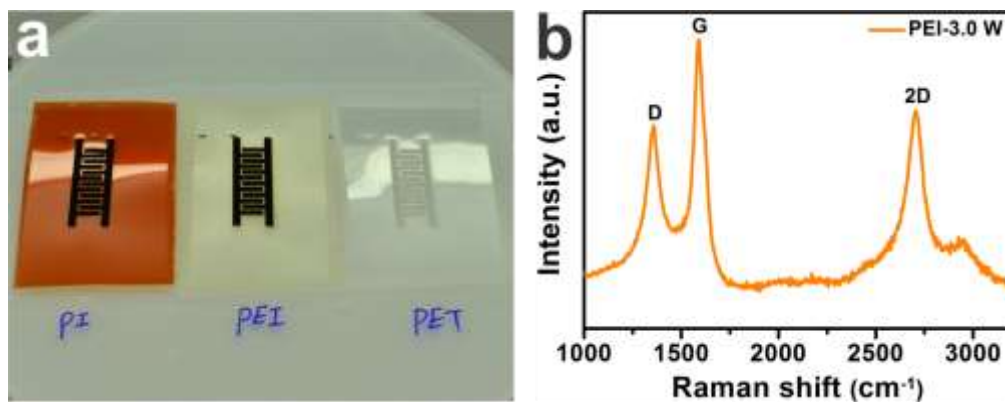
**Supplementary Figure 8 | TGA characterizations of LIG-3.6 W, PI and graphene oxide (GO) in argon.** Compared to GO, which significantly decomposes at ~ 190 °C, LIG is stable at > 900 °C. PI starts to decompose at 550 °C.



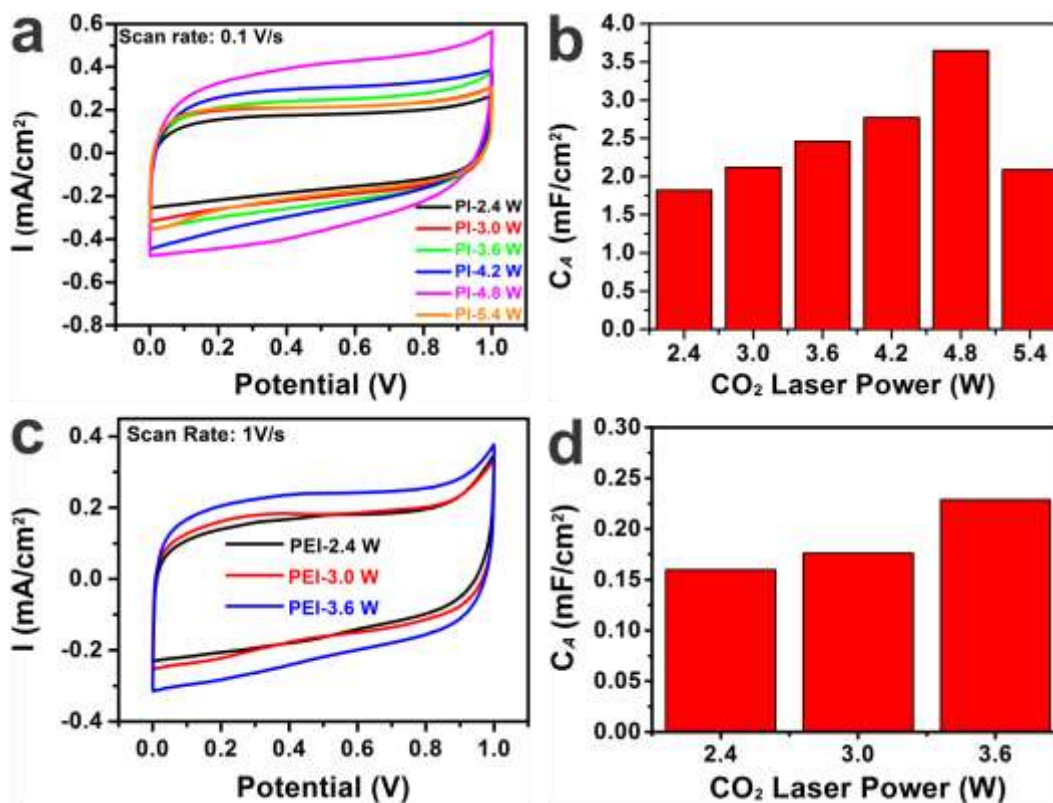
**Supplementary Figure 9 | Correlation of threshold laser power to scan rate.** The threshold power shows a linear dependence on the scan rate. Conditions indicated by the shaded area lead to laser graphitization.



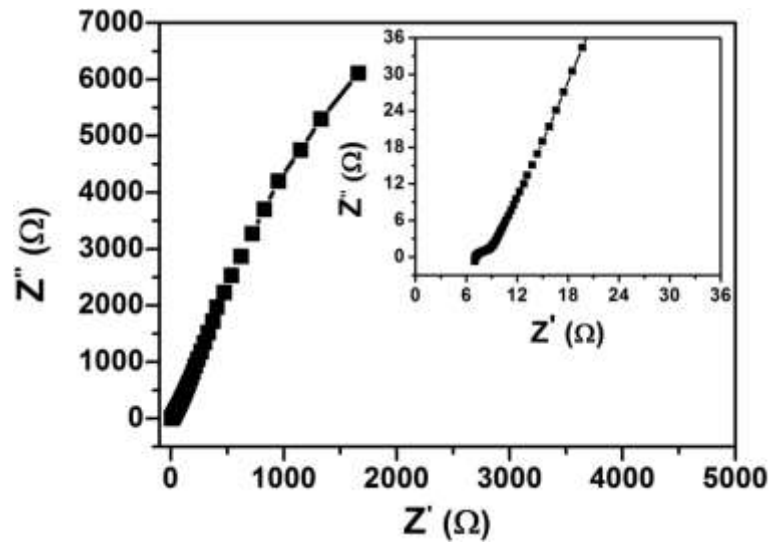
**Supplementary Figure 10 | Characterizations of backsides of LIG films.** **a**, Scheme of the backsides of LIG films peeled from PI substrates. **b**, **c**, **d**, SEM images of backsides of LIG films obtained at laser powers of **b** 2.4 W; **c**, 3.6 W; and **d**, 4.8 W. All of the scale bars are 10  $\mu\text{m}$ . The images show increased pore size as the laser power was increased.



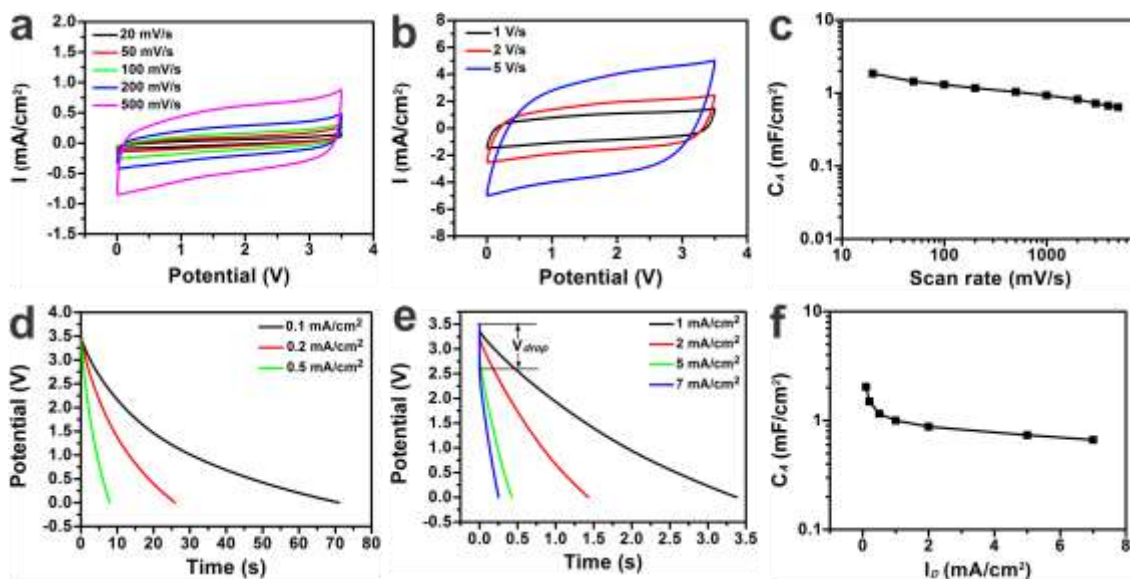
**Supplementary Figure 11 | Characterization of LIG from different polymers. a,** A photograph of patterns induced by lasers on different polymers (PI, PEI and PET) at laser power of 3.0 W. Note that the only two polymers that blackened in this way were PI and PEI. **b,** Raman spectrum of PEI-derived LIG obtained with a laser power of 3.0 W.



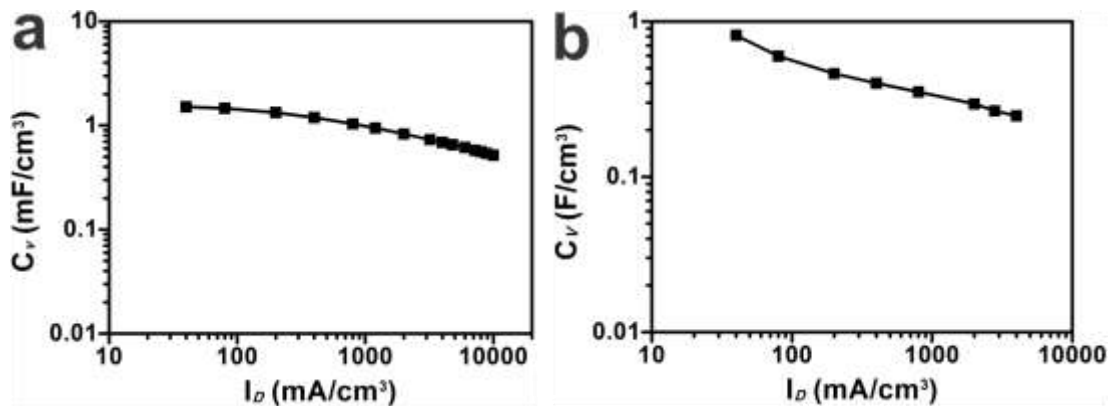
**Supplementary Figure 12 | Electrochemical characterizations of LIG-MSCs obtained from PI and PEI using different laser powers in 1 M H<sub>2</sub>SO<sub>4</sub>.** **a**, Comparison of CV curves of LIG-MSCs obtained from PI at scan rates of 100 mV·s<sup>-1</sup>. **b**, Specific areal capacitances of LIG-MSCs obtained from PI, calculated from CC curves at current densities of 0.2 mA·cm<sup>-2</sup>, as a function of the laser power. **c**, Comparison of CV curves of LIG-MSCs obtained from PEI at scan rates of 1 V·s<sup>-1</sup>. **d**, Specific areal capacitances of LIG-MSCs obtained from PEI, calculated from CC curves at a current density of 0.2 mA·cm<sup>-2</sup>, as a function of the laser power. Compared to PEI derived LIG-MSCs, LIG-MSCs obtained from PI have ~10 × higher capacitances prepared at the same laser powers.



**Supplementary Figure 13 | Impedance spectroscopy of LIG-MSCs obtained from PI using a laser power of 4.8 W in 1 M H<sub>2</sub>SO<sub>4</sub>. Equivalent series resistance is as low as 7  $\Omega$  obtained at a high frequency range.**

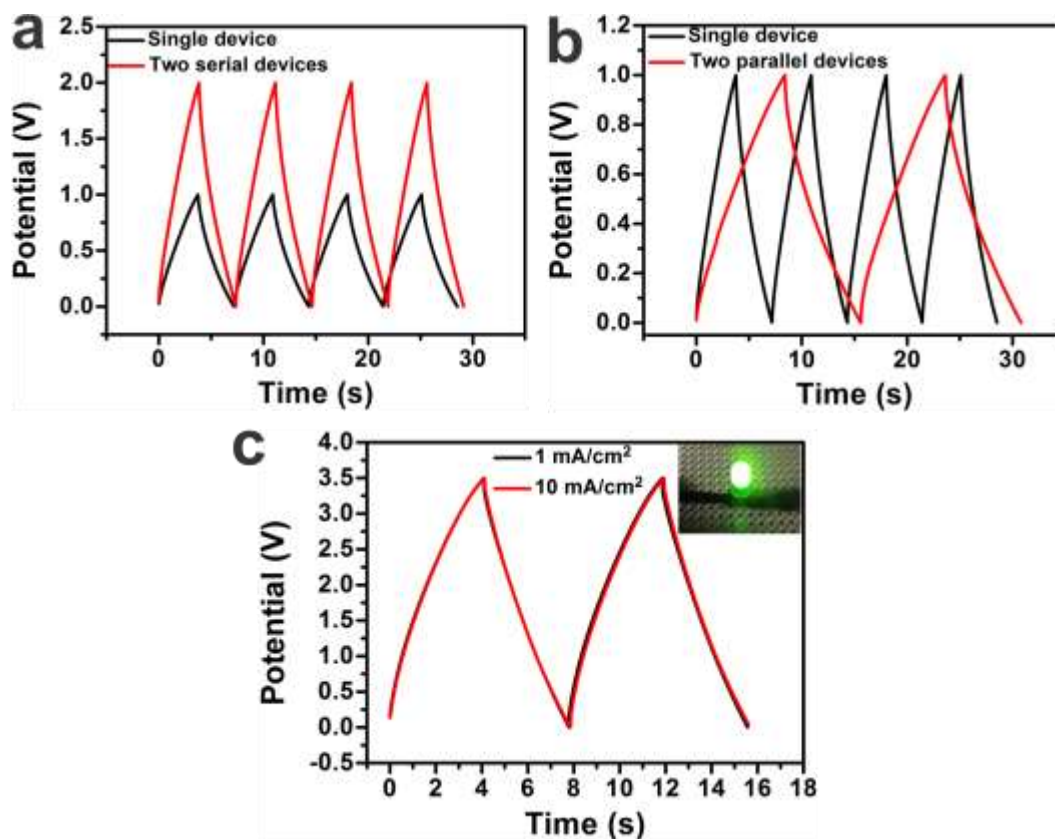


**Supplementary Figure 14 | Electrochemical characterizations of LIG-MSCs obtained with laser power of 4.8 W in BMIM-BF<sub>4</sub>.** **a** and **b**, CV curves of LIG-MSCs at scan rates from 20 mV·s<sup>-1</sup> to 5 V·s<sup>-1</sup>. **c**, Specific areal capacitances vs. scan rates. **d** and **e**, CC curves of LIG-MSCs at discharge current densities from 0.1 mA·cm<sup>-2</sup> to 7 mA·cm<sup>-2</sup>. The voltage drop is shown graphically in **e**. **f**, Specific areal capacitances vs. discharge current densities.

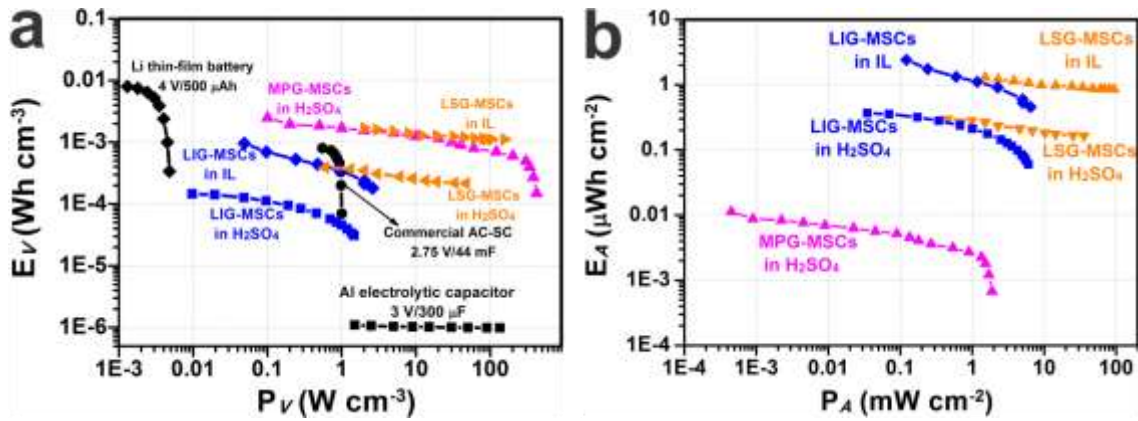


**Supplementary Figure 15 | Comparison volumetric capacitances, calculated from CC curves, of LIG-MSCs in aqueous electrolyte and ionic liquid (IL). a, Specific volumetric capacitances as a function of discharge current densities in 1 M H<sub>2</sub>SO<sub>4</sub>. b, Specific volumetric capacitances as a function of discharge current densities in BMIM-BF<sub>4</sub>.**

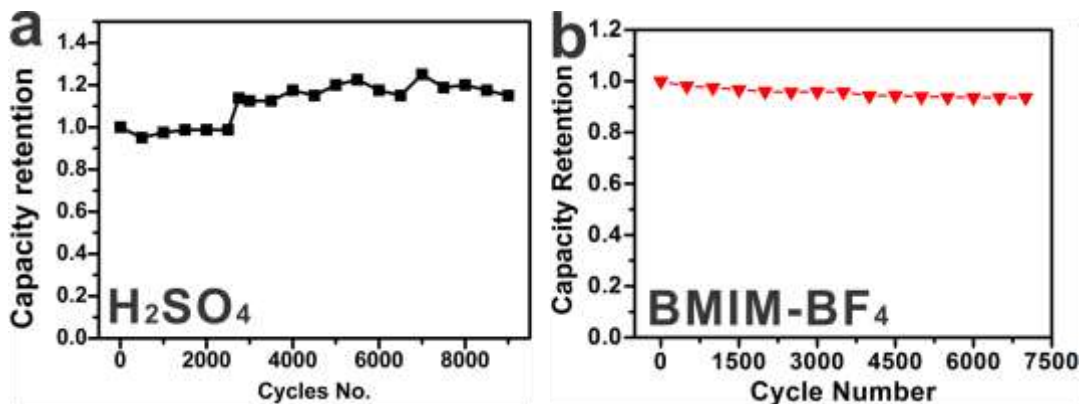




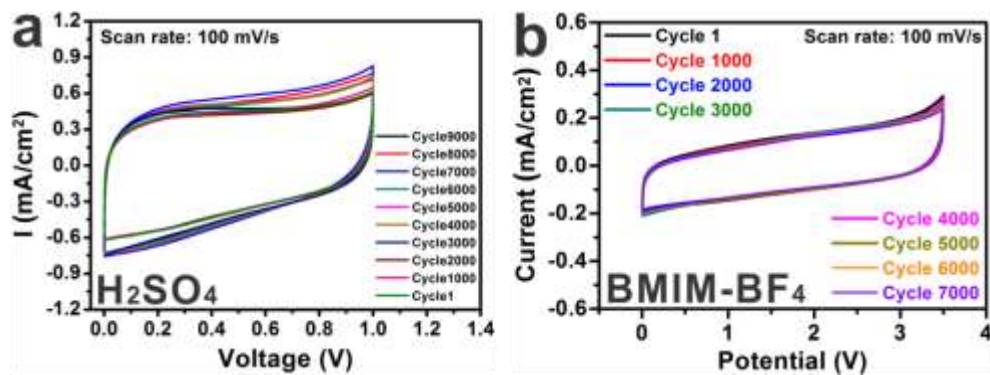
**Supplementary Figure 16 | Electrochemical performance of LIG-MSCs in series/parallel combinations.** Electrolyte for devices in **a** and **b** is 1 M H<sub>2</sub>SO<sub>4</sub>, and for devices in **c** it is BMIM-BF<sub>4</sub>. **a**, CC curves of two tandem LIG-MSCs connected in series with the same discharge current density of 1 mA·cm<sup>-2</sup>. The operation potential window is doubled in serial configuration. **b**, CC curves of two tandem LIG-MSCs in parallel assembly with the same discharge current density of 1 mA·cm<sup>-2</sup>. In this configuration capacitance is almost doubled. **c**, CC curves of single LIG-MSCs and 10 parallel LIG-MSCs at discharge current densities of 1 mA·cm<sup>-2</sup> and 10 mA·cm<sup>-2</sup>, respectively. Current density increases by a factor of 10 with 10 parallel single devices. Inset is a lighted LED powered by 10 parallel LIG-MSCs.



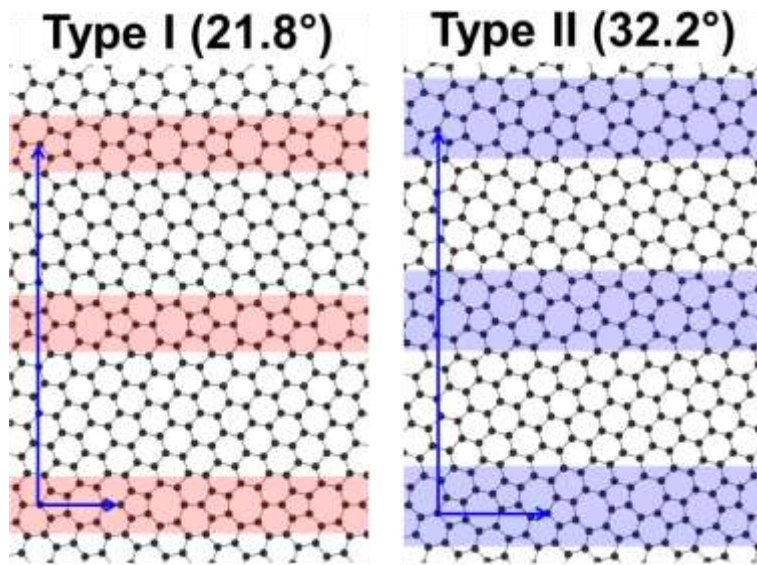
**Supplementary Figure 17 | Comparison Ragone plots of different energy storage devices. a,** Specific volumetric energy and power densities of energy storage devices. **b,** Specific areal energy and power densities of LIG-MSCs and LSG-MSCs. Data were reproduced from references<sup>2,3</sup>.



**Supplementary Figure 18 | Capacity retention of LIG-MSCs constructed with LIG-4.8 W in 1 M H<sub>2</sub>SO<sub>4</sub> and ionic liquid (BMIM-BF<sub>4</sub>).** **a**, Capacitance, calculated from CV curves at a scan rate of 100 mV·s<sup>-1</sup>, increases to 114% of the original value after 2750 cycles, and then retains almost the same value after 9000 cycles. **b**, Capacitance, calculated from CV curves at a scan rate of 100 mV·s<sup>-1</sup>. The capacitance degrades to 95.5% of original value after 1000 cycles, and then stabilizes at 93.5% after 7000 cycles.



Supplementary Figure 19 | CV curves of LIG-MSCs obtained with laser power of 4.8 W in 1M  $\text{H}_2\text{SO}_4$  (a) and  $\text{BMIM-BF}_4$  (b). The curves were obtained at a sweep rate of  $100 \text{ mV}\cdot\text{s}^{-1}$  after every 1000 cycles.


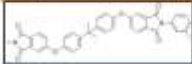
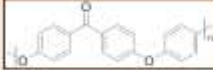
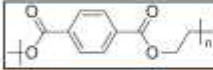



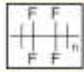

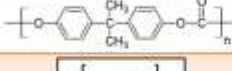
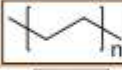
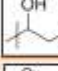
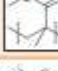




**Supplementary Figure 20 | Atomic structure of the calculated polycrystalline graphene sheets.** The arrows indicate the unit cell, and the grain boundary regions are shaded. Numbers show two types of misorientation angles ( $21.8^\circ$  and  $32.2^\circ$ ) between grains.

## Supplementary Tables

<b>Materials</b>	<b>Carbon (%)</b>	<b>Oxygen (%)</b>	<b>Nitrogen (%)</b>
<b>Polyimide</b>	<b>70.5</b>	<b>22.5</b>	<b>7.0</b>
<b>LIG-1.2 W</b>	<b>72.2</b>	<b>20.3</b>	<b>7.5</b>
<b>LIG-1.8 W</b>	<b>74.7</b>	<b>18.2</b>	<b>7.1</b>
<b>LIG-2.4 W</b>	<b>97.3</b>	<b>2.5</b>	<b>0.2</b>
<b>LIG-3.0 W</b>	<b>95.5</b>	<b>4.1</b>	<b>0.4</b>
<b>LIG-3.6 W</b>	<b>94.5</b>	<b>4.9</b>	<b>0.6</b>
<b>LIG-4.2 W</b>	<b>94.0</b>	<b>5.5</b>	<b>0.5</b>
<b>LIG-4.8 W</b>	<b>92.3</b>	<b>6.9</b>	<b>0.8</b>
<b>LIG-5.4 W</b>	<b>91.3</b>	<b>7.7</b>	<b>1.0</b>

**Supplementary Table 1| Summary of atomic percentage of elements in raw material (PI) and LIG derived from different laser powers. All of the data was obtained by high-resolution XPS scans.**

Full Name	Symbols	Unit	Graphitized?
Kapton Polyimide	PI		Yes
Ulse Polyetherimide	PEI		Yes
Polyether ether ketone	PEEK		No
Polyethylene terephthalate	PET		No
Polyethylene naphthalate	PEN		No
Fluorinated ethylene propylene	FEP		No
Perfluoroalkoxy alkanes	PFA		No
Teflon	PTFE		No
Polystyrene	PS		No
Polycarbonate	PC		No
Polyethylene	PE		No
Polyvinyl alcohol	PVA		No
Poly(methyl methacrylate)	PMMA		No
Acrylonitrile butadiene styrene	ABS		No
Poly(acrylonitrile)	PAN		No

**Supplementary Table 2 | Summary of polymers, their chemical repeat units and their LIG-forming capability. Out of 15 polymers, only PI and PEI were successfully converted to LIG.** Nonaromatic hydrocarbons undergo almost complete degradation without graphitization. Formation of LIG from poly- or heterocyclic structures such as the imide group in PI and PEI polymers favor LIG formation. PAN films are not commercially available and were thus prepared in-house. Though PAN is a precursor to carbon fiber, it does not graphitize well unless heated slowly to permit cyclization and N-extrusion.

## Supplementary References

1. Ma, J., Alfe, D., Michaelides, A. & Wang, E. Stone-Wales defects in graphene and other planar sp(2)-bonded materials. *Phys. Rev. B* **80** (2009).
2. El-Kady, M. F. & Kaner, R. B. Scalable fabrication of high-power graphene micro-supercapacitors for flexible and on-chip energy storage. *Nat. Commun.* **4**, 1475 (2013).
3. Wu, Z. S., Parvez, K., Feng, X. L. & Mullen, K. Graphene-based in-plane micro-supercapacitors with high power and energy densities. *Nat. Commun.* **4**, 2487 (2013).